

# Evaluation of railhead material damage of insulated rail joints due to cyclic wheel loadings

Nirmal Kumar Mandal<sup>a,\*</sup>, Andrea Bracciali<sup>b</sup>, Gianluca Megna<sup>b</sup>

<sup>a</sup> Central Queensland University, Centre for Railway Engineering, Queensland, 4702, Australia

<sup>b</sup> Department of Industrial Engineering, Università Degli Studi di Firenze, Italy

## ARTICLE INFO

### Keywords:

Rail joints  
Composite material endpost  
FEA  
Sub-surface damage  
Cyclic ratchetting  
Elastoplastic material behaviour

## ABSTRACT

Although insulated rail joints (IRJs) are important railway track components and, because of their low bending rigidity, a dynamic wheel impact results as wheels pass over them. Proper attention is needed to address this problem. Focussing on this point, a 3D finite element analysis (FEA) is carried out on IRJs to evaluate on damage analysis of sub-surface railhead material for endpost materials: fiberglass (fb), nylon 66 (ny), and polytetrafluoroethylene (ptfe). A cyclic vertical wheel load up to a total of 2000 cycles in non-Hertzian pressure form is applied at the wheel/rail contact patch on an IRJ. The residual longitudinal stress damage parameter is considered to rank the endpost material based on sub-surface railhead damage. It exhibits a new pattern described as 'vertical flat type' for a depth up to 8 mm initially and, as the cyclic loading increases, the vertical flat pattern damage changes to an 'inclined flat type' pattern.

## 1. Introduction

Insulated rail joints (IRJs) are important railway track components for railway operations and train control. The IRJs are necessary for designing modern railway signalling systems that require railway track circuits to be created in track made up of continuously welded rail and where the design does not include axle counters. They are usually used for locating trains through electrical signal blocks and for detecting broken rails. The endposts are used in IRJs to electrically insulate one length of rail from another to create electrical signal blocks.

Focussing on insulation materials used in railway IRJs, the performance of the endpost materials between two rail ends is the primary purpose of this article. For other insulation applications in rail joints, analysis should also be carried out into items such as insulating material placed between the rail web and joint bars, and the bushing material applied around the bolts. In addition, there are other issues requiring examination including determining which insulation materials are good for providing reliable railway electrical signalling, for resisting peeling damage, and for reducing railhead steel chipping out problems. And also which insulation materials are good for minimising sub-surface damage so as to resist sub-surface railhead crack initiation.

Usually, composite materials, polymers, thermosetting plastics, thermoplastics, etc. are used as endpost materials. The popular polymers

and composite materials are polytetrafluoroethylene (ptfe), fibreglass (fb), nylon (ny), melamine formaldehyde, polystyrene, polycarbonate, aramid (kevlar 49), polyvinyl chloride, urea formaldehyde, polypropylene, carbon fibre-epoxy, etc. In IRJs, fb is the most commonly used endpost material in Australia. Other popular alternative endpost materials are ny and ptfe. Because of rail end gaps at IRJs, the bending rigidity is less, and a stress singularity occurs with associated damage to the endpost itself and the adjacent railhead material (Fig. 1). Therefore, it is required to pay attention to providing a proper geometric design of IRJs, focussing on the endpost materials and other geometric parameters to reduce stress states.

For increasing the service life of a rail, it is important to know detailed information on plastic deformation and damage to the rail top surface and sub-surface material. For the 60 kg head hardened rail used for heavy-haul coal lines in the Rockhampton area in Queensland Australia, the yield strength is 780 MPa [1]. The peak values of the contact pressure load imposed by the wheels are well above the yield strength of the rail material. As a result, severe plastic deformation and damage occur at the rail top surface and its underlying sub-surface. As the cyclic loading increases, the damage problems accumulate [2,3]. The residual stresses resulting when there is no load on the rail joints can be a measure of the top surface and sub-surface damage of the rail material.

\* Corresponding author.

E-mail address: [n.mandal@cqu.edu.au](mailto:n.mandal@cqu.edu.au) (N.K. Mandal).

<https://doi.org/10.1016/j.wear.2023.204966>

Received 6 November 2022; Received in revised form 25 March 2023; Accepted 16 May 2023

Available online 18 May 2023

0043-1648/© 2023 Elsevier B.V. All rights reserved.

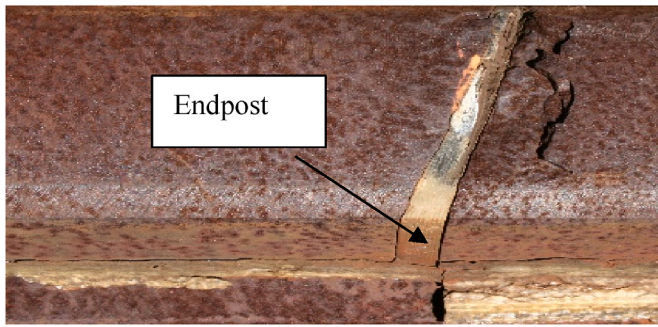


Fig. 1. A failure mode of an insulated rail joint: material degradation and chipping out.

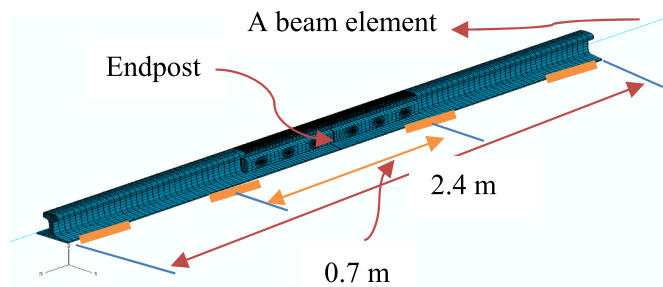


Fig. 2. FEA global model of IRJ centrally suspended between sleepers.

It is essential to select some important damage parameters to assess the damaging nature of railhead in the vicinity of IRJs. A few of the damage parameters are residual von-Mises stress, residual vertical stress, residual longitudinal stress, and so on. Because of the bending and reverse bending of IRJs due to wheel loadings, rail material in the vicinity of IRJs experiences severe longitudinal stress and strain, so, residual longitudinal stress is considered as a damage parameter in this paper. The damage parameters such as residual vertical stress and strain components [4,5] are employed to determine the damage trends of subsurface railhead material due to cyclic loadings. Effects of cyclic loadings on sub-surface damage of railhead material are worth quantifying. Mandal et al. [4] noticed a sub-surface railhead damage pattern caused by the three endpost materials for different cyclic wheel loadings. It was found that, under initial loading cycles, sub-surface damage was of a vertical flat type. As the loading cycles increased, the damage pattern changed to a horizontal bell-shaped type for several damage parameters. This is due to residual vertical strain and von-Mises stress. It is worth investigating the effects of other damage parameters such as residual vertical stress [5], longitudinal stress, and strain. In the following section, a thorough review of related papers is carried out to establish the development in this area.

The mechanical behaviour of IRJs is also important. Soft endpost materials are used in IRJs and some research studies have been carried out focussing on the impact factor evolved due to short wavelength defects, height mismatch, etc., at IRJs [6–9]. The researchers quantified P1 and P2 impact forces generated while a wheel was passing over IRJs. Other research studies relating to IRJs have focused on railhead degradation [10–12], mechanical behaviour [13–19], endpost thickness [20], contact modelling [21], condition monitoring [22–23], bolt looseness [24–27], and vibration and noise [28]. Focussing on the lipping of railhead top surface material, Beaty et al. [11] articulated that endposts with higher compressive strength and harder rail steel can improve the IRJ performance. However, the thickness of the endpost produced no effects on lipping damage.

Discussing problems with bolted rail joints, but not railhead sub-

surface damage, Zhu et al. [24] pointed out that longer joint bar designs performed similarly to the standard joint bar designs. However, a thicker joint bar reduced vertical IRJ displacements and upper fillet stresses compared to standard designs. A larger bolt loading could work similarly to the vertical IRJs displacement and upper fillet stresses [25], but stresses on bolt holes increased. Gallou et al. [14] studied the use of reinforcement by strap rails or I-beams attached to the sleepers between and parallel to the running rails containing the IRJs and showed that this stiffened the track structure and significantly reduced the vertical displacement and formation of dip angles at IRJs.

Through the literature search, it is revealed that there are many studies focused on various issues of IRJs. They are relating to contact modelling, assessing the generation of noise and vibration, shape optimisation of the rail ends, and reinforcement of track beside the IRJs to reduce vertical displacement. There are very few studies focused on sub-surface damage due to the effects of endpost materials. Most recently, it was established that a particular pattern of sub-surface damage occurred for certain kinds of damage parameters. The damage pattern may depend on damage parameters. Therefore, it is necessary to carry out a detailed study of sub-surface damage of railhead material with IRJs using some popular endpost materials (fb, ny and pte), benchmarking the mechanical behaviour of ny and pte against the most commonly used fb. As the effects of endpost materials on mechanical behaviour and railhead and sub-surface material damage due to cyclic wheel loading are not yet available fully, a detailed rail sub-surface damage pattern due to various damage parameters is deemed important for product design and development purposes. In this paper, residual longitudinal stress and strain damage parameters are considered to quantify a new damage pattern of the sub-surface railhead material in the vicinity of IRJs due to cyclic wheel loadings focussing on two research questions. The simulation results obtained by finite element analysis are compared with laboratory testing results.

The research questions of this study are.

1. Rather than resisting the problems of flow of railhead steel across the rail end gap, how do endpost materials of IRJs control sub-surface railhead damage?
2. Can residual longitudinal stress and strain damage parameters exhibit a different damage shape rather than a 'horizontal bell' curve type for sub-surface railhead material in the vicinity of IRJs?

## 2. FEA modelling

This study is completed in two stages: Stage 1 for finite element analysis (FEA) and Stage 2 for laboratory verification. A 3D FEA (ABAQUS) is conducted to model IRJs considering a global model and a sub-model for local damage analysis. Section 2.1 presents a global FEA modelling of a 5 mm endpost thickness IRJ, and a sub-model of part of the railhead in the vicinity of the IRJ. As the applied wheel loadings produce a contact stress level over the yield point of the head-hardened rail material, a non-linear isotropic/kinematic hardening material behaviour was considered for the contact zone of the wheel/rail interface. Sections 3 and 4 demonstrate the material modelling and the simulated results and Section 5 provides verification of FEA simulation results using longitudinal strains measured experimentally at the rail top surface, 150 mm away from the endpost. Section 6 presents the relevant conclusions.

### 2.1. Rail joint global and sub-model

A 12 m long piece of rail with an IRJ in the middle is considered in this study. Igwemezie and Nguyen [29] considered a similar rail piece for their study. This length is deemed sufficient when considering boundary conditions of a finite section of rail [16,29]. Two beam models, each 4.8 m long, are connected to the ends of the 2.4 m long solid rail joint model by equation constraints in ABAQUS. This ensures

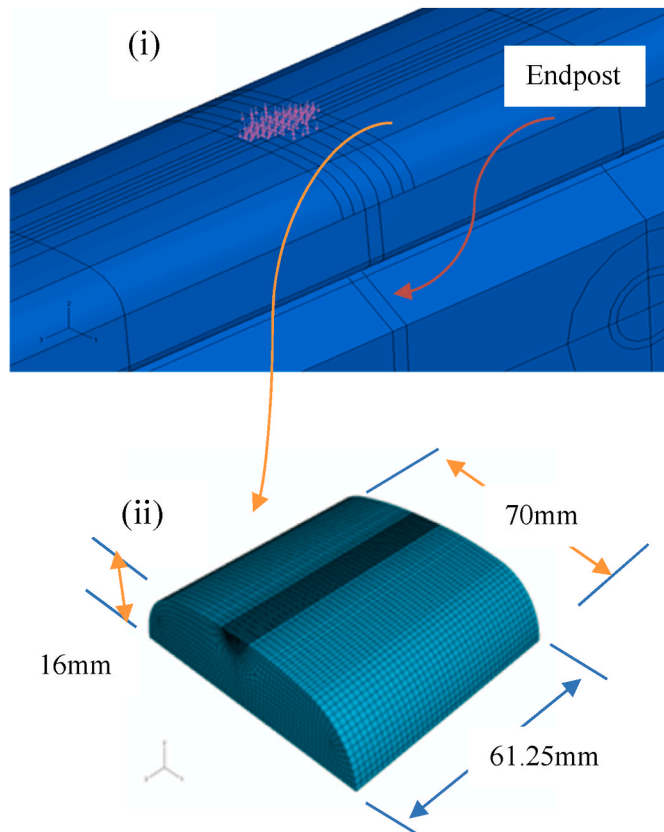


Fig. 3. Zoomed in view of IRJ: (i) a portion of global model showing location of sub-model and loading on IRJ, (ii) sub-model.

Table 1  
Rail steel and endpost material properties [18].

Name	Young's Modulus (MPa)	Poisson's Ratio
Head hardened rail steel	207000	0.3
Fibreglass (fb)	45000	0.19
Nylon 66 (ny)	1590	0.39
PTFE (ptfe)	400	0.46

Table 2  
Elastic-plastic properties of rail top surface material (the high mesh density part shown in Fig. 2) [18,34,36].

$\sigma_y$ (MPa)	$K_{\infty}$ (MPa)	$b'$	$c$ (MPa)	$\gamma$
780	152	3.97	393000	8.3

zero displacements and rotation of beams and rail relative to one another and that all six DOFs are transferred from the solid rail model to the beam models. It also ensures that the excitation is provided by the wheels passing over the IRJ, while all six DOFs are nullified at the end of the beam model, ensuring a valid FEA simulation [3]. The Australian Standard 1085.12 [30] is considered to model the 60 kg/m rail profile and position the rail with a 1/20 rail-cant. Other parameters are: 5 mm endpost thickness, 6 bolt joint plates, IRJ is centrally suspended between two adjacent sleepers (Fig. 2) with 0.7 m centre to centre sleeper spacing. The rail foot of the IRJ is considered to be fixed, simulating rigid support from the sleepers [31,32]. The endpost is connected to the rail ends by a tie constraint available in ABAQUS [32]. Fig. 3 (i) shows the 174 kN dynamic wheel loading in pressure form imposed on the IRJ considering a non-Hertzian contact theory. A contact patch size of 26 mm (the major axis, 2a) x20mm (the minor axis 2 b) on the crown

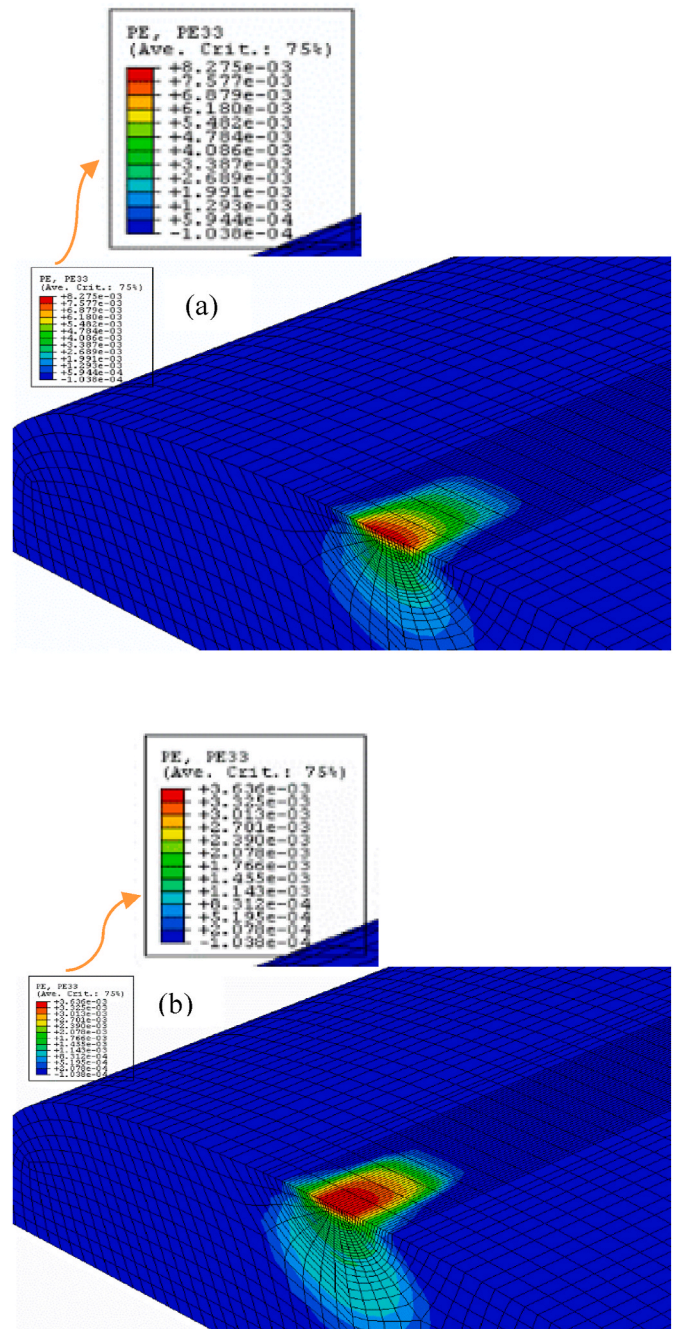
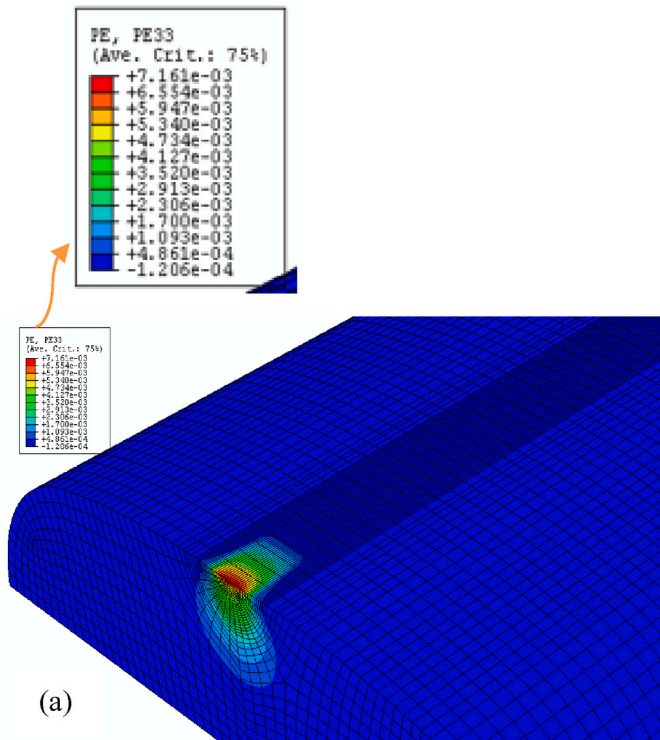


Fig. 4. Contour plots of PE33 for ptfе endpost under: (a) loaded; and (b) unloaded conditions.

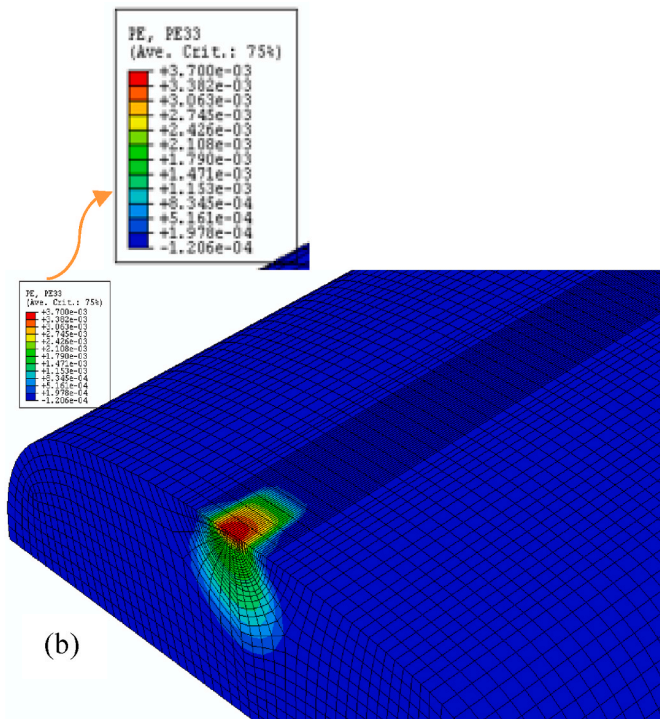
Table 3  
Residual longitudinal strain PE33: for ptfе (Fig. 4), fb (Fig. 5), ny (not shown).

	Loading	Unloading
PE33 of ptfе	0.00827	0.00363
PE33 of fb	0.00716	0.00370
PE33 of ny	0.01086	0.004007

surface of one rail end was considered. The non-linearity of the ellipsoidal pressure distribution was simulated using a stepwise pressure variation with the highest peak pressure of 2500 MPa, followed by 610MPa and 73 MPa, the two lower pressure peaks employed gradually away from the top of the ellipsoidal pressure distribution on the wheel/rail contact patch to reflect the non-Hertzian pressure



(a)



(b)

Fig. 5. Contour plots of PE33 for fb endpost under: (a) loaded; and (b) unloaded conditions.

distribution. A bolt load  $P_b$  of 200 kN was calculated based on Equation (1) considering a bolt torque  $T$  of 1050 Nm, the bolt diameter  $D$  of 24 mm, and a bolt torque moment coefficient ( $k_b = 0.19–0.25$ ) [33]. The bolt load is applied axially on the cross-section of each of the bolts. ABAQUS's part and section modules are used to construct the IRJ model and apply homogeneous section and elastic-plastic material properties

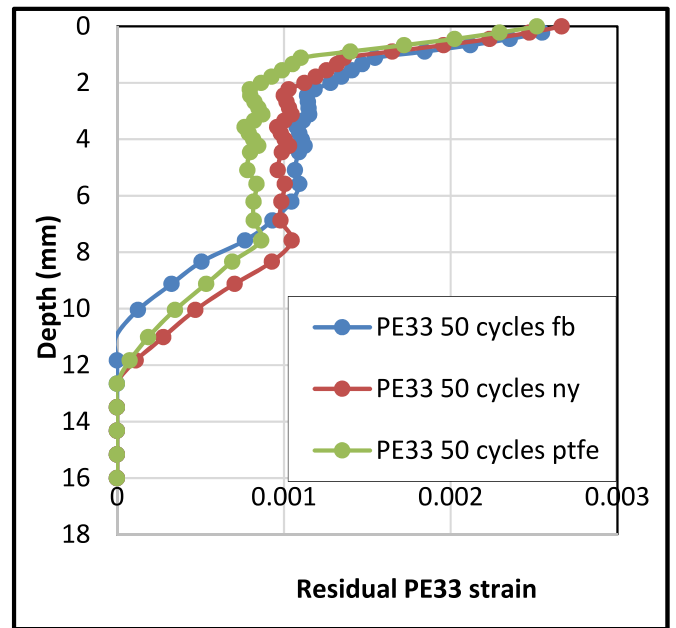


Fig. 6. Residual longitudinal strains at various railhead sub-surface depths after 50 cycles of wheel loadings for three endpost materials.

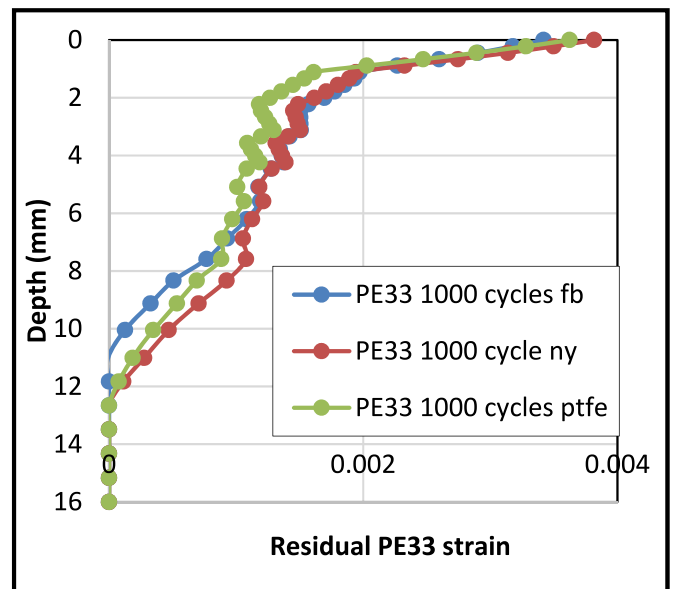


Fig. 7. Residual longitudinal strains at various railhead sub-surface depths after 1000 cycles of wheel loadings for three endpost materials.

respectively. The top critical area of the head of the rail (the dark part seen in Fig. 2) is defined with high mesh density (i.e., fine mesh) to account for elastic-plastic material deformation. The high mesh density part is constructed separately in ABAQUS and connected to the other parts of the IRJ model by tie constraints. For the critical zone in the vicinity of the rail end, a bias seeding option in Abaqus was considered for maintaining node density for making fine mesh. Therefore, the size of the elements varies from 0.5 mm to 1.5 mm in the critical zone. For non-critical locations, the elements are larger, being from 3 mm to 5 mm. Those other parts of the IRJ model are elastic. Table 1 presents the Young's Modulus and Poisson's Ratio of the rail steel and endpost materials. Table 2 illustrates the elastic-plastic material properties of the top surface of the head-hardened rail. In Table 2,  $\sigma_y$  is the yield strength,

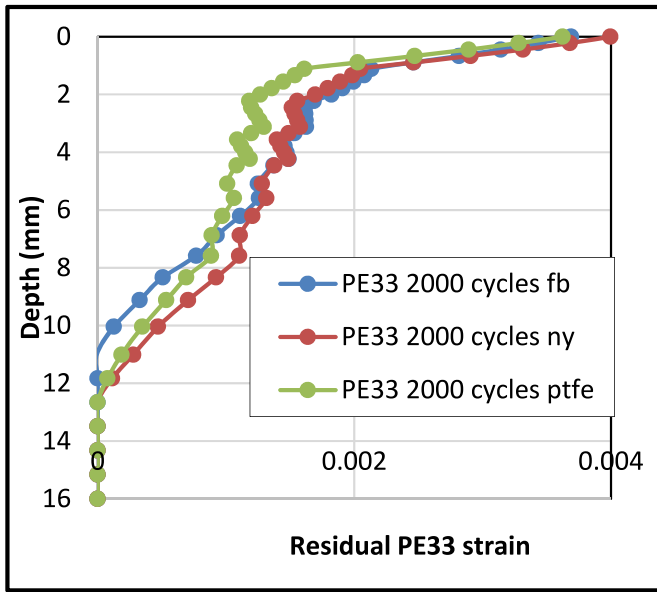


Fig. 8. Residual longitudinal strains at various railhead sub-surface depths after 2000 cycles of wheel loadings for three endpost materials.

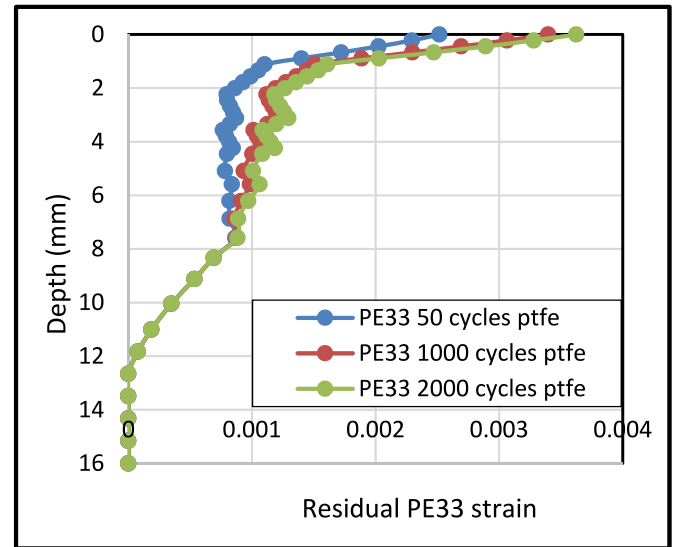


Fig. 10. Residual longitudinal strains at various railhead sub-surface depths after 50, 1000 and 2000 cycles of wheel loadings for ptfe endpost material.

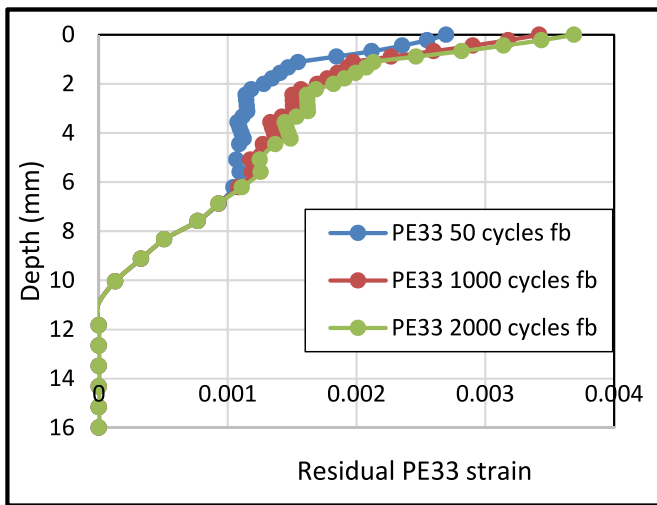


Fig. 9. Residual longitudinal strains at various railhead sub-surface depths after 50, 1000 and 2000 cycles of wheel loadings for fb endpost material.

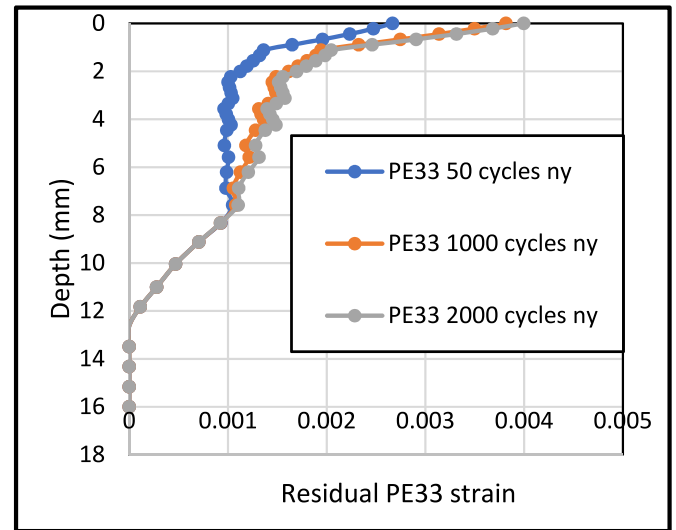


Fig. 11. Residual longitudinal strains at various railhead sub-surface depths after 50, 1000 and 2000 cycles of wheel loadings for ny endpost material.

$K_{\infty}$  is the maximum change in the size of the yield surface,  $b'$  is the rate at which the size of the yield surface changes as plastic straining develops,  $c$  is the kinematic hardening modulus, and  $\gamma$  is the rate at which the kinematic hardening modulus decreases with the increase of plastic deformation. The material constants are collected from the open literature such as Abaqus documentation on material modelling, Bower [34], Ringsberg [35], etc. The parametric analysis of those material constants is carried out focussing on equivalent plastic strain (PEEQ) to see when the ratchetting material behaviour is reduced and a set of material constants was thereby selected (Table 2). This parametric analysis is out of the scope of this study. The material modelling is presented in Section 3.

$$P_b = \frac{T}{K_b D} \quad (1)$$

The directions indicated in Fig. 2 are in the global co-ordinate system positive directions, with '1', '2' and '3' as the lateral track direction, the vertical direction the longitudinal direction, respectively.

The simulation analysis is carried out statically in two steps. In step 1, all boundary conditions and bolt loads are applied. In step 2, a total of 2000 cycles of a dynamic cyclic wheel load of 174 kN in pressure form is applied in 4 s with a 0.001 s time increment. The wheel/rail contact force obtained from the contact-impact analysis was idealised and applied normal to the railhead surface in such a way that the maximum peak pressure of 2500 MPa occurred at the edge of one of the railhead ends at the endpost air gap symmetric to the rail cross section. This peak pressure load ensures ratchetting material behaviour as the load factor  $P_0/k = 5.5$  where  $P_0 = 2500$  MPa and the yield stress in shear  $k = 450$  MPa. Hence the load factor is more than the ratchetting limit of 4.68 [34]. A similar peak pressure of 2000 MPa was employed [35] elsewhere.

It should be noted that, at the time of contact-impact, the contact pressure was therefore distributed across the endpost and onto both railheads at the IRJ rail discontinuity as shown in Fig. 3(i). The dynamic wheel load on the rail is greater than the static wheel load of 150 kN. Fig. 3(ii) presents a sub-model. Mandal et al. [8] indicated that the

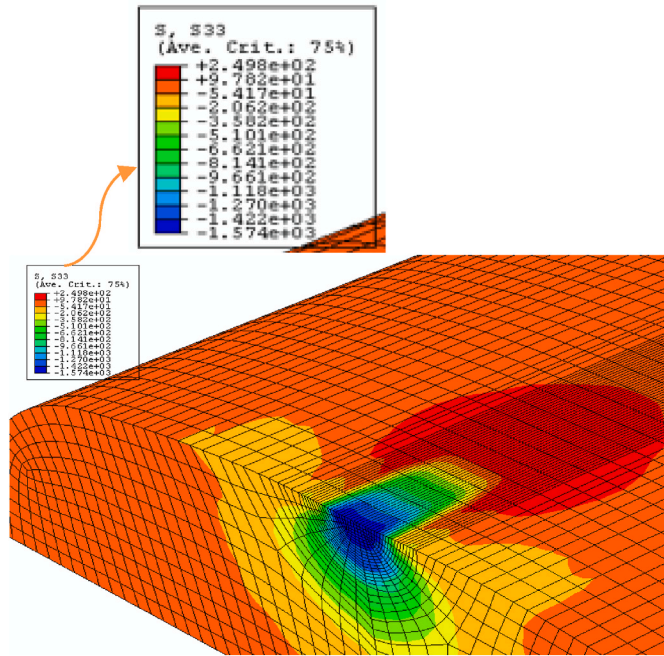


Fig. 12. Contour plot of S33 for loaded conditions due to ptfе endpost material at the end of 2000 loading cycles.

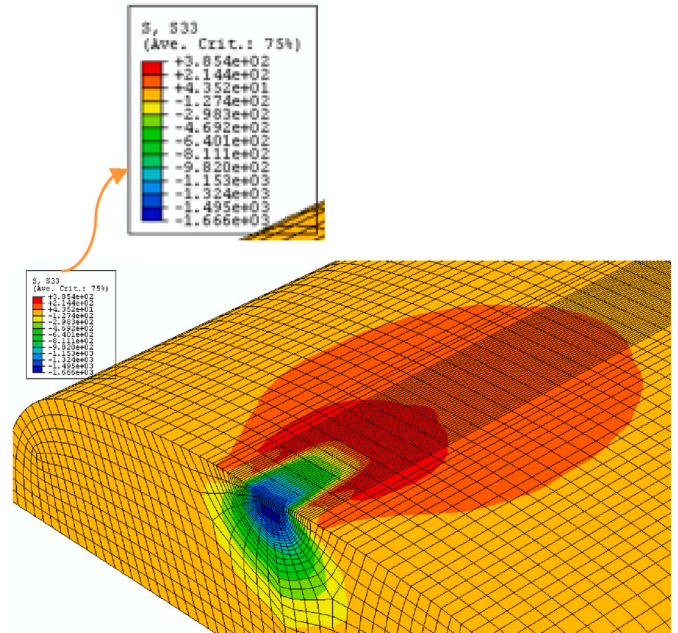


Fig. 14. Contour plot of S33 for loaded conditions due to ny endpost material at the end of 2000 loading cycles.

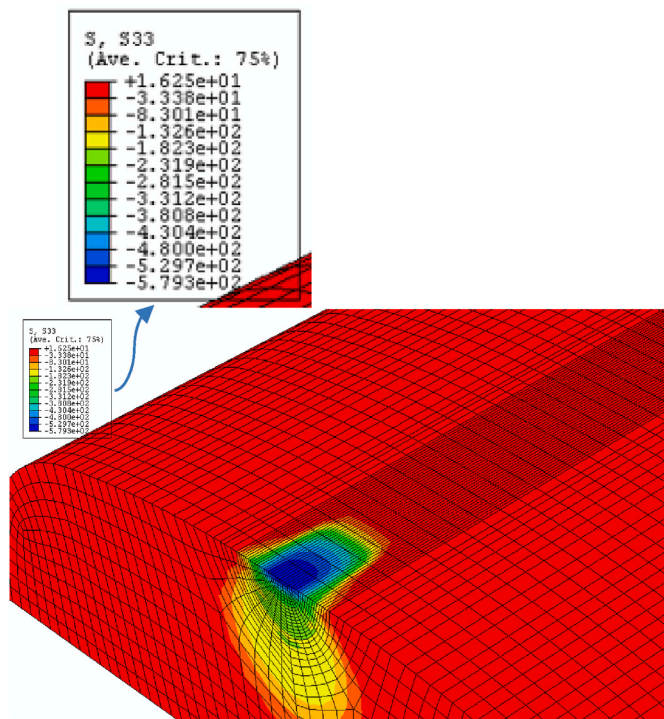


Fig. 13. Contour plot of S33 for unloaded conditions due to ptfе endpost material at the end of 2000 loading cycles.

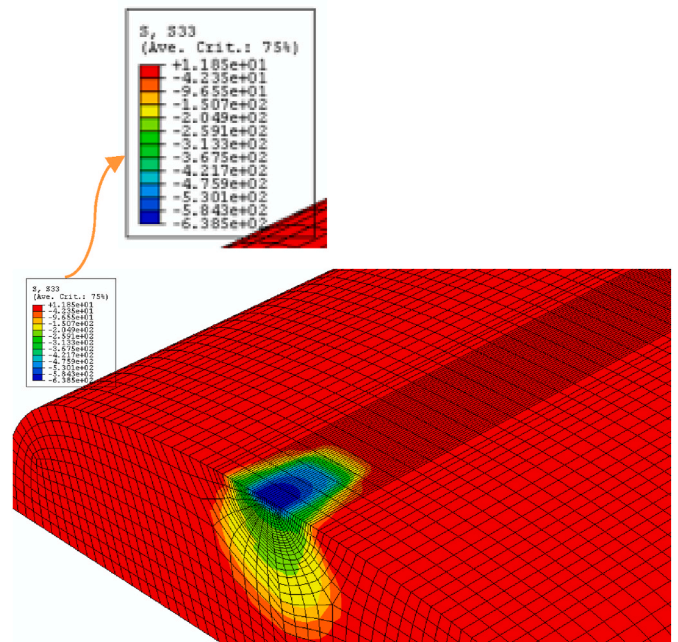


Fig. 15. Contour plot of S33 for unloaded conditions due to ny endpost material at the end of 2000 loading cycles.

degree of increase of dynamic wheel loads over static wheel loads depends on track design parameters, speed and irregularities of the rail and proposed a dynamic impact factor which is the ratio of these two forces. In this study, a dynamic impact factor of 1.16 is considered. This impact factor [8] evolves because the study is based upon the Rockhampton to Blackwater coal route railway with 26.6 axle load and 80 km/h speed.

In this simulation, an eight-node fully integrated tri-linear brick

element (C3D8) was considered in the solid modelling zone in the mesh module. It is free from volumetric locking. Therefore, it does not create any problem during plastic deformation. In the job module, the simulation was completed statically to obtain the displacement degrees of freedom at the nodes of the global model which were then used to run a sub-model of rail separately. The simulation results from the sub-model are presented in Section 4.

As this study focuses on detailed damage analysis of railhead sub-surface material, a local FEA modelling strategy called sub-modelling is a more appropriate and accurate simulation type for this purpose. A critical section close to the top surface of the railhead at the free rail ends

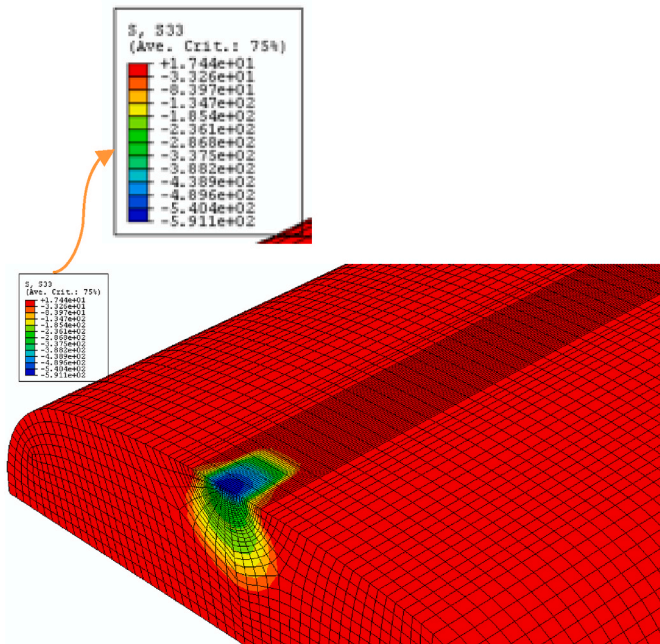


Fig. 16. Contour plot of S33 for unloaded conditions due to fb endpost material at the end of 2000 loading cycles.

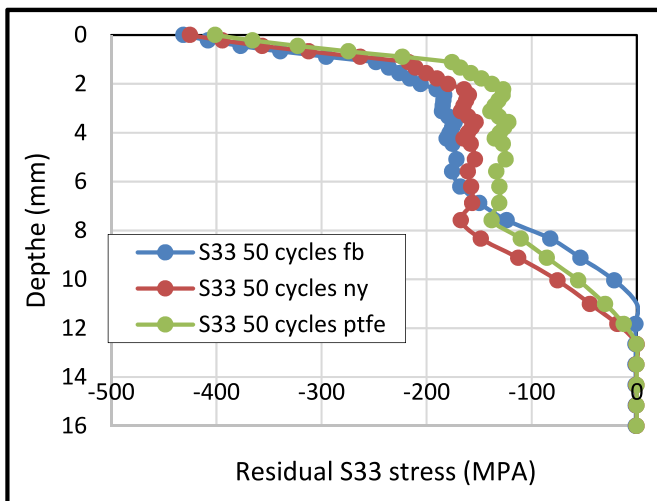


Fig. 17. Residual longitudinal stress (S33) at various railhead sub-surface depths after 50 cycles of wheel loadings for three endpost materials.

of the IRJ (Fig. 3 (ii)) is considered for sub-modelling analysis, keeping the same magnitude of x, y, and z coordinates along with the dimensions of the sub-model. Four sub-model meshes were employed and, with a mesh convergence study, an optimum mesh (sub-model 3 or mesh 3) (Fig. 3(ii)) with 46166 nodes and 41600 elements was selected for the analysis. The nodes and element numbers of other meshes respectively are 13,338 and 11,492 for mesh 1, 29,376 and 26,180 for mesh 2, and 90,240 and 83,444 for mesh 4. The displacement DOFs from the global model were applied to the sub-model boundary and the full analysis was rerun as it had been in the global model to produce simulation results output files. The computation efficiency in the sub-modelling analysis increased significantly. The average time taken to run the global model is about 24 h. However, the time taken to run the sub-model is less than an hour. The sub-model analysis is much more efficient.

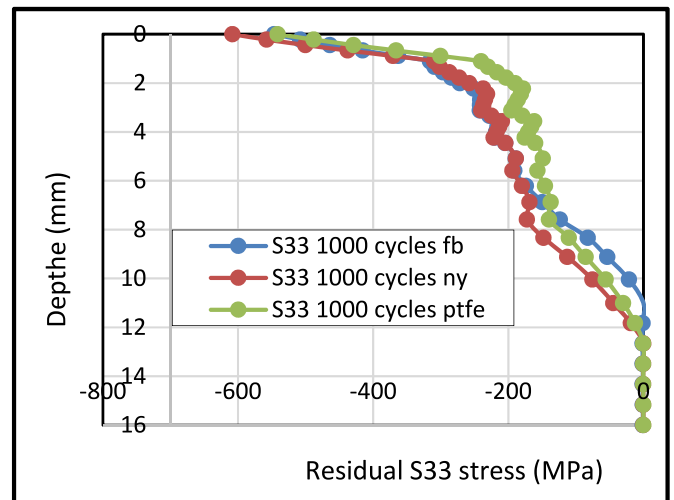


Fig. 18. Residual longitudinal stress (S33) at various railhead sub-surface depths after 1000 cycles of wheel loadings for three endpost materials.

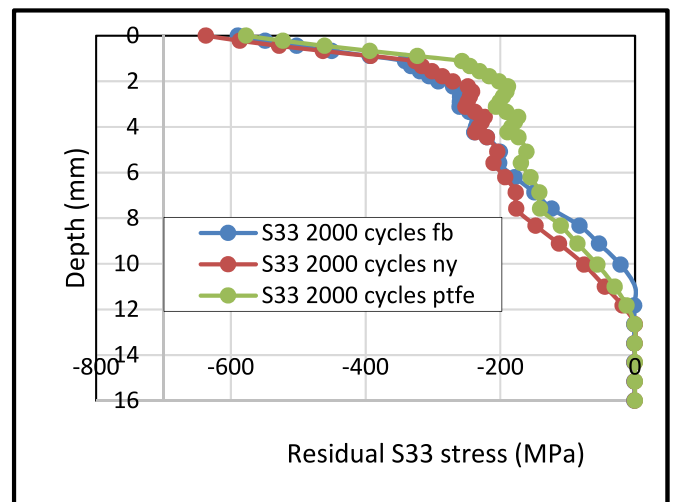


Fig. 19. Residual longitudinal stress (S33) at various railhead sub-surface depths after 2000 cycles of wheel loadings for three endpost materials.

### 3. Material modelling

In the following section, the flow rule, evolution laws and yield surface in plastic material behaviour are discussed briefly. The material models relate to the constitutive equations of stress and strain responses.

*A yield surface:* relates to either the von Mises or Hill yield surface. It is independent of the pressure stress generally for all metals. The von Mises yield surface defines isotropic yielding.

*A flow rule:* ensures that inelastic deformation occurs as there is no pure elastic material behaviour.

*Evolution laws:* These laws define the hardening and control how yield and flow definitions change as inelastic deformation occurs.

The contact stress level at the contact zone is higher than that of the yield point of the rail material. Therefore, a nonlinear isotropic/kinematic hardening material model, called combined material in Abaqus, is used to mimic the material behaviour (Table 2) for cyclic loadings. It is based on incremental plasticity theory in which the mechanical strain rate is decomposed into two parts: an elastic part and a plastic part. For the railhead top surface (fine mesh area, Fig. 2), an elasto-plastic material modelling concept is therefore employed in this paper. This theory is related to a yield surface, evolution laws and a flow rule. The

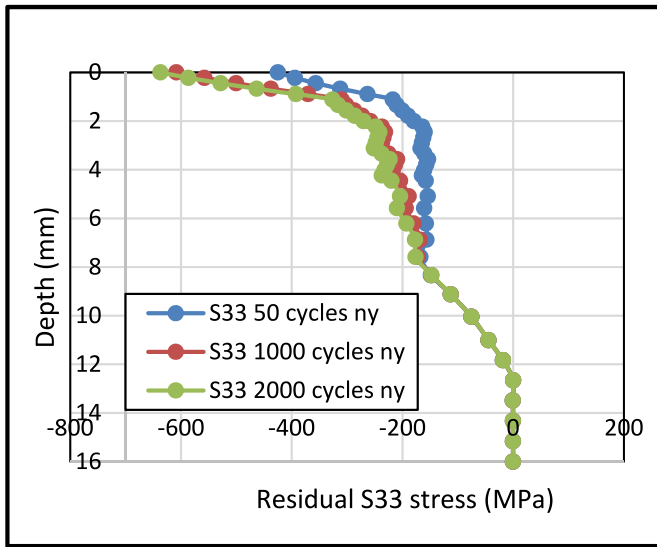


Fig. 20. Residual longitudinal stress (S33) at various railhead sub-surface depths after 50, 1000 and 2000 cycles of wheel loadings for ny endpost materials.

nonlinear isotropic/kinematic hardening material model is good for Bauschinger effects, ratchetting and relaxation, and plastic shakedown. The isotropic and kinematic laws are coupled. As such, the yield surface is free to change its shape and size and free to move in stress space. The isotropic law is also responsible for decay in the ratchetting rate. The yield stress is generally defined by a von Mises yield surface, a kinematic hardening rule and associated plastic flow rules. For other than the fine mesh areas, elastic material properties are used.

A von Mises yield surface function is defined as:

$$\varphi(\sigma, X, K) = \sqrt{\frac{3}{2}}|\tau_{dev}| - K - \sigma_y \tag{2}$$

with  $\tau_{dev} = \sigma_{dev} - X_{dev}$ ,  $|\tau_{dev}| = \sqrt{\tau_{dev} : \tau_{dev}}$

where  $|\tau_{dev}|$  is the equivalent von Mises stress,  $\sigma_{dev}$  is the deviatoric stress tensor (defined as  $\sigma_{dev} = \sigma - pI$ , where  $\sigma$  is the stress tensor,  $p$  is the equivalent pressure stress and  $I$  is the identity tensor),  $\sigma_y$  is the yield stress,  $K$  is the drag stress,  $X_{dev}$  is the deviatoric part of the back stress tensor and the operator ‘:’ defines the contraction  $x:y = x_{ij}y_{ij}$ .

The non-linear hardening model includes both isotropic and kinematic hardening. The isotropic hardening law can be stated as:

$$\dot{K} = \lambda b \left(1 - \frac{K}{K_\infty}\right) \tag{3}$$

This law indicates a decay in the ratchetting rate where  $\lambda$  is the plastic multiplier,  $K_\infty$  is the saturated drag stress due to isotropic hardening and  $b$  governs the initial rate of isotropic hardening. Both  $b$  and  $K_\infty$  are material parameters.

A non-linear kinematic hardening model relies on the steady accumulation of plastic strain. The law can be stated as:

$$\dot{X} = \lambda \left( c \sqrt{\frac{2}{3}} n_{dev} - \gamma X \right) \tag{4}$$

where  $n_{dev} = \frac{\tau_{dev}}{|\tau_{dev}|}$  and  $c$  and  $\gamma$  are material parameters.

#### 4. Results and discussions

The simulation data from the FEA sub-modelling analysis are employed to rank the performance of the three endpost materials considering the level of railhead sub-surface damage. Two damage

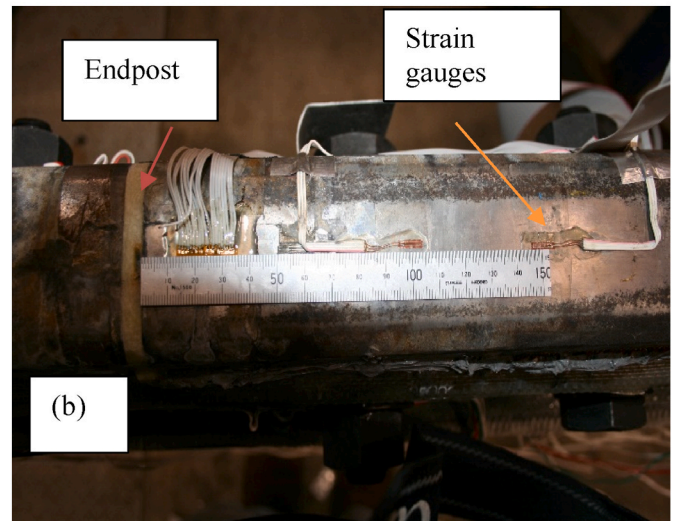
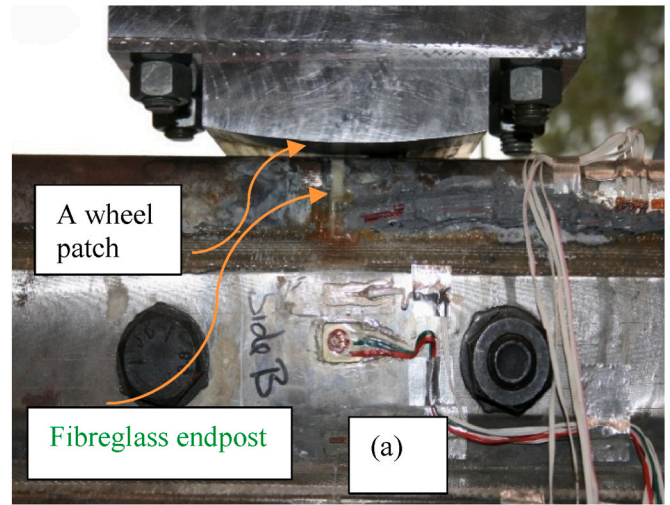


Fig. 21. Laboratory testing: (a) loading on insulated rail joint, (b) location of strain gauge at the top surface of the rail (150 mm away from endpost) used for verification.

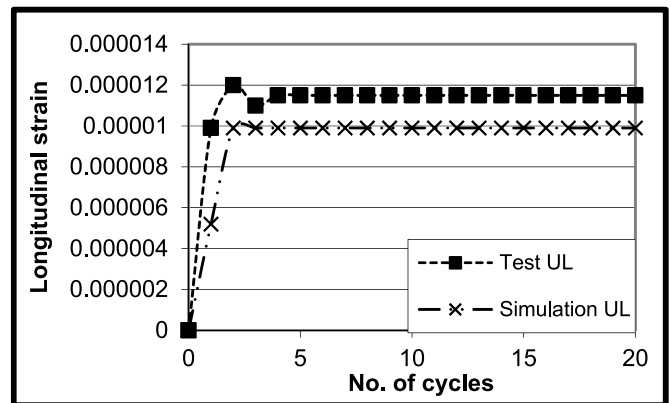


Fig. 22. Longitudinal strains on rail top material at 150 mm away from the endpost.

parameters are considered to quantify this damage, namely residual longitudinal plastic strain (PE33) and residual longitudinal stress (S33) for 50, 1000 and 2000 vertical wheel load cycles. In this section, simulation results based on residual longitudinal strains are initially presented followed by residual longitudinal stress results. Although the FEA model is reported in previous studies [5], these new results can be meaningful for railway engineering practitioners for the evaluation of the geometric design of IRJs and hardness distributions of railhead material.

#### 4.1. Strain results

For pure elastic metal behaviour, the strain is fully recoverable. When performing an elastic-plastic analysis, it is assumed that the plastic strain dominates the deformation and the elastic strain is small. Therefore, for assessing the permanent deformation of materials forming a plastic zone, plastic strain signatures are a good way to illustrate this. A zero value of plastic strain ensures material behaviour is fully elastic. Because of cyclic loading, the plastic strain is changing over each cycle, and values of the plastic strain when there is no load (i.e., the residual component) are used to quantify the plastic zone.

Fig. 4 shows contour plots of PE33 for loaded and unloaded conditions at the end of 2000 loading cycles due to 5 mm ptfе endpost material. It shows that the top railhead surface in the vicinity of IRJ is severely strained. The maximum value of the strain at the rail end is about 0.00827 for loaded conditions (Fig. 4(a)). At no load conditions, the residual component of it is about 0.00363 (Fig. 4(b)). For other endpost materials, the corresponding values at the end of 2000 cycles of wheel loading are placed in Table 3 including those of ptfе. At the top of the railhead close to the rail end, the residual plastic strain PE33 for ptfе and fb (Fig. 5) is similar and less than that of ny material (Table 3). The best to worst performance ranking can be in the order of ptfе, fb and ny. For sub-surface depths, it can be different.

Fig. 6, on the other hand, shows the variation of residual PE33 in the sub-surface of the railhead material for 50 loading cycles when using all three endpost materials (fb, ny and ptfе). It is seen that, at the very shallowest sub-surface depth (<1 mm), the values of PE33 are changing linearly in a similar fashion for all endpost materials. This damage pattern can be referred to as an ‘inclined flat type’ (Pattern I). For a sub-surface depth of 1–7 mm, the damage pattern is a ‘vertical flat type’ (Pattern II), illustrating that the influence of the ptfе endpost on minimising sub-surface damage of railhead material is better compared to that of ny and fb. The best to worst ranking of these three endpost materials for reducing sub-surface damage after 50 loading cycles is ptfе, ny and then fb. For the higher depth of 8–12 mm, the damage pattern is again an ‘inclined flat type’ (Pattern III) with a new best to worst ranking of fb, ptfе and ny relating to reducing damage. This suggests that, for different depths, the sub-surface material damage pattern is different. At greater sub-surface depths, the residual plastic strain values are zero, ensuring material behaviour is fully elastic. Some of the sub-surface damage patterns are similar to those observed in recent literature [5] for residual PE22. However, rankings of the effect of the three endpost materials are different.

For higher loading cycles of 1000 cycles or 2000 cycles, damage patterns of Pattern I and Pattern III remain the same. However, there is a significant change in Pattern II type damage. It changes from the ‘vertical flat type’ to an ‘inclined flat type’ (modified Pattern II), indicating that ptfе endpost material performs better compared to the performances of the other two (Figs. 7 and 8). The damage parameter of PE33 illustrates a different Pattern II damage type than that stated in Ref. [5]. It also provides a slightly different ranking of the endpost materials compared to that for lower cyclic loadings.

The above observation of how the damage pattern of a ‘vertical flat type’ changed to an ‘inclined flat type’ can be presented clearly by displaying sub-surface damage for each particular endpost material for three scenarios of 50, 1000, and 2000 loading cycles (Figs. 9–11). From

these plots, it is evident that, at 50 loading cycles, the Pattern II damage pattern is present. As the loading cycles increase, the Pattern II damage pattern changes to the modified Pattern II type damage. At the same time, it shows that more plastic deformation occurs initially (from 50 to 1000 cycles) and then it reduces from 1000 to 2000 cycles. It is evident that decay in the ratchetting rate is happening with an increase in loading cycles.

This research considered only the vertical impacts with no longitudinal creep force. The traction effects at the contact patch can change the mechanical behaviour of railhead material and it can influence the vertical flat-type damage patterns. The subsequent future research direction will consider both vertical and longitudinal forces at the contact interface to investigate the effects of creep forces on the sub-surface damage patterns.

#### 4.2. Stress analysis

In this section, another damage parameter called residual longitudinal stress (S33), is presented focussing on railhead sub-surface damage in terms of plastic deformation which is forming a plastic zone. A similar type of presentation is carried out to that of PE33. Fig. 12 shows a contour plot of S33 for fully loaded conditions at the end of 2000 loading cycles for ptfе endpost material. It shows that the top railhead surface is severely stressed and magnitudes reach up to 1574 MPa, well above the yield point of the head hardened rail material of 780 MPa [1] used for IRJs. At no load conditions, the residual component of S33 is about 579.3 MPa (Fig. 13). For the other endpost material of ny, the contour plot presents the longitudinal stress level as 1666.0 MPa for loaded conditions (Fig. 14) and 636.5 MPa for unloaded conditions (Fig. 15). For fb endpost material, the corresponding values are 1806.0 MPa for loaded conditions (not shown) and 591.1 MPa for unloaded conditions (Fig. 16). Therefore, regarding the rail top material damage in the vicinity of IRJs, the endpost material best to worst ranking is ptfе, fb, and ny. This is similar to that obtained from residual PE33 consideration.

Figs. 17–19 show S33 distributions at railhead sub-surface depths for three loading scenarios of 50, 1000, and 2000 cycles with Fig. 17 for 50 cycles for all three materials, Fig. 18 for 1000 cycles and Fig. 19 for 2000 cycles. Similar observations of patterns are evident from these figures. In Fig. 17, all three damage patterns (Pattern I, Pattern II, Pattern III) are present. At higher loading cycles (Fig. 18 and 19), Pattern I and Pattern III are the same, and a similar change in Pattern II as was observed previously for strains again occurs with Pattern II changing to a modified Pattern II. A clear difference in the performance of endpost materials is shown with ptfе as the best performing endpost material followed by ny, then fb. At high loading cycles, the performance of fb and ny with regard to sub-surface damage is similar. This study shows that this is not a general case. For the same ny endpost material, the sub-surface distributions of residual S33 for different loading conditions are shown in Fig. 20. This also shows that, at lower loading cycles (50 cycles), the sub-surface damage pattern is Pattern II type. As the loading cycles are increasing, the Pattern II type changes to a modified Pattern II type, as observed before. A decay of ratchetting rate results with the increase in loading cycles.

### 5. Validation of simulation results

It is also necessary to validate any simulation results with the results from laboratory tests incorporating the same input and support conditions, including loading (cyclic wheel loading of 174 kN in pressure form) and other boundary conditions. Fig. 21(a) shows the testing arrangement incorporating a loading patch representing a wheel of radius 425 mm for a fibreglass endpost. Fig. 21(b) shows the longitudinal strain gauge located on top of the rail 150 mm away from the endpost rail gap and this is used to obtain the longitudinal strain signatures for validation. The simulation results are compared with the laboratory test results over 20 cycles (Fig. 22). A reasonable correlation

is achieved. This suggests that the results presented previously can be trusted. The variation of these two results is due to some non-uniform load application conditions. In testing, a force of 174 kN was vertically applied cyclically on the IRJ. In the simulation, a stepwise pressure form equivalent to a 174 kN force was employed. This can be a possible cause for variations in the two results.

## 6. Conclusions

A detailed stress analysis was carried out on a 6 bolt IRJ of standard Australian design considering the performance of different endpost materials by applying wheel loadings up to 2000 cycles that yield contact stress over the yield strength of the rail steel. A wheel load of 174 kN with a peak pressure load of 2500 MPa was considered without any longitudinal creep force at the contact zone. Ratchetting material behaviour of railhead material can be expected under these conditions. The following conclusions can be made based on the observations of this study.

1. at sub-surface depth 1–7 mm, a ‘vertical flat type’ damage pattern (Pattern II type) is observed for all damage parameters due to 50 loading cycles.
2. as the loading cycles increase, the ‘vertical flat damage’ pattern II changes and a modified Pattern II type damage is observed.
3. the occurrence of Pattern I type damage (<1 mm depth) and Pattern III type damage (8–12 mm depth) are not loading cycle dependent.
4. as the number of loading cycles increase, a decay in ratchetting rate is observed.
5. among the three endpost materials considered, ptfе is the best material relating to less sub-surface railhead material damage.

## Funding Authorities

No fundings.

## Declaration of competing interest

There is no conflict of interest arising from this publication and related study.

## Data availability

Data will be made available on request.

## Acknowledgments

Thanks go to Prof. M. Dhanasekar for his meticulous guidance to finish this research. Tim McSweeney, Adjunct Research Fellow, CRE is thankfully acknowledged for his advice at many stages of this ongoing study.

## References

- [1] AS 1085.1, Railway Track Material: Steel Rails, 2002 (Standards Australia).
- [2] N.K. Mandal, Ratchetting damage of railhead material of gapped rail joints with reference to free rail end effects, *Proc. Inst. Mech. Eng. - Part F J. Rail Rapid Transit* 231 (2) (2017) 211–225.
- [3] N.K. Mandal, FEA to assess plastic deformation of railhead material damage of insulated rail joints with fibreglass and nylon endposts, *Wear* 366–367 (2016) 3–12.
- [4] N.K. Mandal, R. Lewis, Z. Wen, Quantification of sub-surface railhead material damage due to composite endpost materials of insulated rail joints for cyclic wheel loadings, *Eng. Fail. Anal.* 113 (2020), 104562.
- [5] N.K. Mandal, M. Spiryagin, Q. Wu, Z. Wen, S. Stichel, FEA of mechanical behaviour of insulated rail joints due to vertical cyclic wheel loadings, *Eng. Fail. Anal.* 133 (2022), 105966.
- [6] E. Soylemez, K. Ciloglu, Influence of track variable and product design on insulated rail joints, *J. Transport. Res. Board* (2016) 1–10, <https://doi.org/10.3141/2545-01>.
- [7] Y.Q. Sun, C. Cole, M. Spiryagin, Study on track dynamic forces due to rail short-wavelength dip defects using rail vehicle-track dynamics simulations, *J. Mech. Sci. Technol.* 27 (3) (2013) 629–640.
- [8] N.K. Mandal, M. Dhanasekar, Y.Q. Sun, Impact forces at dipped rail joints, *Journal of Rail and Rapid Transit* 230 (1) (2016) 271–282.
- [9] I. Grossoni, S. Iwnicki, Y. Bezin, C. Gong, Dynamics of a vehicle-track coupling system at a rail joint, *Journal of Rail and Rapid Transit* 229 (4) (2015) 364–374.
- [10] H.M. El-sayed, M. Lotfy, H.N. El-din Zohny, H.S. Riad, A three dimensional finite element analysis of insulated rail joints deterioration, *Eng. Fail. Anal.* 91 (2018) 201–215.
- [11] P. Beaty, B. Temple, M.B. Marshall, R. Lewis, Experimental modelling of lipping in insulated rail joints and investigation of railhead material improvements, *Journal of Rail and Rapid Transit* 230 (4) (2016) 1375–1387.
- [12] N. Zong, M. Dhanasekar, Minimization of railhead edge stresses through shape optimization, *Eng. Optim.* 45 (9) (2013) 1043–1060.
- [13] M. Gallou, M. Forest, A. El-Hamalawi, C. Hardwick, Assessing the deflection behaviour of mechanical and insulated rail joints using finite element analysis, *Journal of Rail and Rapid Transit* 232 (9) (2018) 2290–2308.
- [14] M. Gallou, B. Temple, C. Hardwick, M. Frost, A. El-Hamalawi, Potential for external reinforcement of insulated rail joints, *Journal of Rail and Rapid Transit* 232 (3) (2018) 697–708.
- [15] T.M. Bandula-Heva, M. Dhanasekar, Failure of discontinuous railhead edges due to plastic strain, *Eng. Fail. Anal.* 44 (2014) 110–124.
- [16] N.K. Mandal, M. Dhanasekar, Sub-modelling for the ratchetting failure of insulated rail joints, *Int. J. Mech. Sci.* 75 (2013) 110–122.
- [17] N.K. Mandal, Ratchetting damage of railhead material of gapped rail joints with reference to free rail end effects, *Journal of Rail and Rapid Transit* 231 (2) (2017) 211–225.
- [18] N.K. Mandal, Plastic ratchetting of railhead material in the vicinity of insulated rail joints with wheel and thermal loads, *Wear* 330–331 (2015) 540–553.
- [19] N.K. Mandal, On the low cycle fatigue failure of insulated rail joints (IRJs), *Eng. Fail. Anal.* 40 (2014) 58–74.
- [20] N.K. Mandal, Ratchetting of railhead material of insulated rail joints (IRJs) with reference to endpost thickness, *Eng. Fail. Anal.* 45 (2014) 347–362.
- [21] N. Yang, A. Boogaard, Z. Wei, J. Liu, R. Dollevoet, Z. Li, Numerical study of wheel-rail impact contact solutions at an insulated rail joint, *Int. J. Mech. Sci.* 138–139 (2018) 310–322.
- [22] M. Oregui, S. Li, A. Nunez, Z. Li, R. Carroll, R. Dollevoet, Monitoring bolt tightness of rail joints using axle box acceleration measurements, *Struct. Control Health Monit.* 24 (2017) 1–15.
- [23] M. Oregui, M. Molodova, A. Nunez, R. Dollevoet, Z. Li, Experimental investigation into the condition of insulated rail joints by impact excitation, *Exp. Mech.* 55 (2015) 1597–1612.
- [24] K. Zhu, Y. Qian, J.R. Edwards, B.O. Andrawes, Finite element analysis of rail end bolt hole and fillet stress on bolted rail joints, *Transport. Res. Rec.: J. Transport. Res. Board* (2017) 33–42.
- [25] K. Zhu, J.R. Edwards, Y. Qian, B. Andrawes, Finite element analysis of the effects of bolt condition on bolted rail joints, *Transport. Res. Rec.: J. Transport. Res. Board* (2016) 36–45.
- [26] J.J. Kalker, Survey of wheel-rail rolling contact theory, *Veh. Syst. Dyn.* 8 (4) (1979) 317–358.
- [27] P. Clayton, M.B.P. Allery, P.J. Bolton Pj, Surface damage phenomena in rails, in: J. Kalousek, R.V. Dukkipati, G.M.L. Gladwell (Eds.), *Proceedings of the Conference on Contact Mechanics and Wear of Rail/wheel Systems*, University of Waterloo Press, Vancouver, British Columbia, 1983, pp. 419–443. July 6–9, 1982.
- [28] N. Yang, A. Boogaard, R. Chen, R. Dollevoet, Z. Li, Numerical and experimental study of wheel-rail impact vibration and noise generated at an insulated rail joint, *Int. J. Impact Eng.* 113 (2018) 29–39.
- [29] J. Igwemezie, A.T. Nguyen, Anatomy of Joint Bar Failures, *Railway Track and Structures*, July 2009, pp. 31–37.
- [30] AS 1085.12, Railway Track Material: Insulated Joint Assemblies, 2002. Standards Australia.
- [31] Z. Wen, G. Xiao, X. Xiao, X. Jin, M. Zhu, Dynamic vehicle-track interaction and plastic deformation of rail at rail welds, *Eng. Fail. Anal.* 16 (4) (2009) 1221–1237.
- [32] E. Kabo, J.C.O. Nielsen, A. Ekberg, Prediction of dynamic train-track interaction and subsequent material deterioration in the presence of insulated rail joints, *Veh. Syst. Dyn.* 44 (Supplement 1) (2006) 718–729.
- [33] Z. Wen, X. Jin, W. Zhang, Contact-impact stress analysis of rail joint region using the dynamic finite element method, *Wear* 258 (7–8) (2005) 1301–1309.
- [34] A.F. Bower, K.L. Johnson, in: J.J. Kalker, et al. (Eds.), *Shakedown, Residual Stress and Plastic Flow in Repeated Wheel-Rail Contact*, Rail Quality and Maintenance for Modern Railway Operation, 1993, pp. 239–249.
- [35] Y.C. Chen, The effect of proximity of a rail end in elastic-plastic contact between a wheel and a rail, *Journal of Rail and Rapid Transit* 217 (3) (2003) 189–201.
- [36] J.W. Ringsberg, Cyclic ratchetting and failure of a pearlitic rail steel, *Fatig. Fract. Eng. Mater. Struct.* 23 (2000) 747–758.